UCRL-JC-125494
PREPRINT

# The Two-Dimensional Structure of Radiative Divertor Plasmas in the DIII-D Tokamak

M. E. Fenstermacher, S. L. Allen, N. H. Brooks, D. A. Buchenauer, T. N. Carlstrom, J. W. Cuthbertson, E. J. Doyle, T. E. Evans, P. M. Garbet, R. W. Harvey, D. N. Hill, A. W. Hyatt, R. C. Isler, G. Jackson, R. A. James, R. Jong, C. C. Klepper, C. J. Lasnier, A. W. Leonard, M. A. Mahdavi, R. Maingi, W. H. Meyer, R. A. Moyer, D. G. Nilson, T. W. Petrie, G. D. Porter, T. L. Rhodes, M. J. Schaffer, R. D. Stambaugh, D. M. Thomas, S. Tugarinov, M. R. Wade, J. G. Watkins, W. P. West, D. G. Whyte, R. D. Wood

This paper was prepared for submittal to the
38th Annual Meeting, American Physical Society Division of Plasma Physics
Denver, Colorado
November 11-15, 1996

October 1996

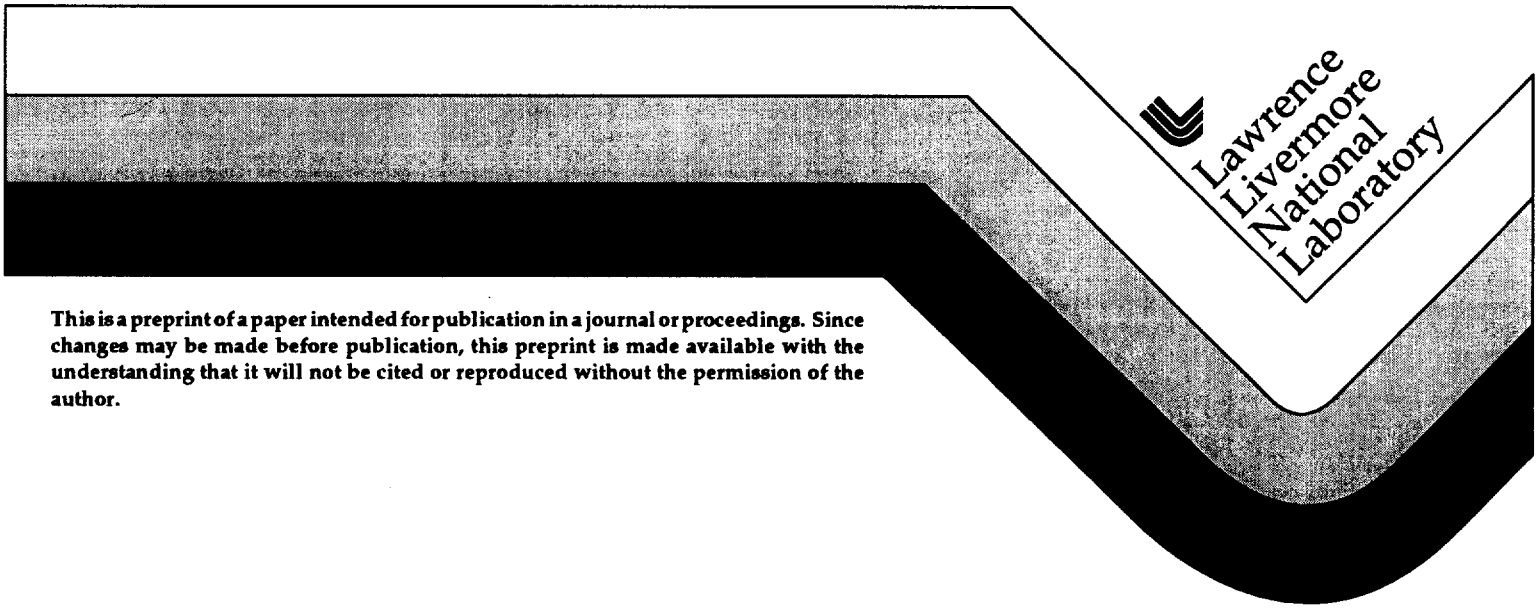


This is a preprint of a paper intended for publication in a journal or proceedings. Since changes may be made before publication, this preprint is made available with the understanding that it will not be cited or reproduced without the permission of the author.

DISCLAIMER

This document was prepared as an account of work sponsored by an agency of the United States Government. Neither the United States Government nor the University of California nor any of their employees, makes any warranty, express or implied, or assumes any legal liability or responsibility for the accuracy, completeness, or usefulness of any information, apparatus, product, or process disclosed, or represents that its use would not infringe privately owned rights. Reference herein to any specific commercial product, process, or service by trade name, trademark, manufacturer, or otherwise, does not necessarily constitute or imply its endorsement, recommendation, or favoring by the United States Government or the University of California. The views and opinions of authors expressed herein do not necessarily state or reflect those of the United States Government or the University of California, and shall not be used for advertising or product endorsement purposes.

# The two-dimensional structure of radiative divertor plasmas in the DIII–D tokamak

M.E. Fenstermacher, S.L. Allen, N.H. Brooks,[a] D.A. Buchenauer,[b] T.N. Carlstrom,[a] J.W. Cuthbertson,[c] E.J. Doyle,[d] T.E. Evans,[a] P.-M. Garbet,[e] R.W. Harvey,[a] D.N. Hill, A.W. Hyatt,[a] R.C. Isler,[f] G. Jackson,[a] R.A. James, R. Jong, C.C. Klepper,[f] C.J. Lasnier, A.W. Leonard,[a] M.A. Mahdavi,[a] R. Maingi,[g] W.H. Meyer, R.A. Moyer,[c] D.G. Nilson, T.W. Petrie,[a] G.D. Porter, T.L. Rhodes,[d] M.J. Schaffer,[a] R.D. Stambaugh,[a] D.M. Thomas,[a] S. Tugarinov,[g] M.R. Wade,[f] J.G. Watkins,[b] W.P. West,[a] D.G. Whyte,[h] R.D. Wood

Lawrence Livermore National Laboratory, P.O.Box 808, Livermore, California. 94550

Recent measurements of the 2–D spatial profiles of divertor plasma density, temperature, and emissivity in the DIII–D tokamak under highly radiating conditions are presented. Data are obtained using a Divertor Thomson Scattering system and other diagnostics optimized for measuring the high electron densities and low temperatures in these detached divertor plasmas ($n_e \leq 10^{21}$ m$^{-3}$, 0.5 eV $\leq T_e$). $D_2$ gas puffing in the divertor increases the plasma radiation and lowers $T_e$ to less than 2 eV in most of the divertor volume. Modeling shows that this temperature is low enough to allow ion-neutral collisions, charge exchange, and volume recombination to play significant roles in reducing the plasma pressure along the magnetic separatrix by a factor of 3 to 5, consistent with the measurements. Absolutely calibrated VUV spectroscopy and 2–D images of impurity emission show that carbon radiation near the X–point, and deuterium radiation near the plates contribute to the reduction in $T_e$. Uniformity of outer leg radiated power (within a factor of 2) along the outer divertor leg, with peak target heat flux on the divertor target

[a] General Atomics, P.O. Box 85608, San Diego, California 92186-9784.
[b] Sandia National Laboratories, Albuquerque, New Mexico.
[c] University of California, San Diego, California.
[d] University of California, Los Angeles, California.
[e] Association EURATOM–CEA sur la fusion, Cadarache, France.
[f] Oak Ridge National Laboratory, Oak Ridge, Tennessee.
[g] TRINITI, Troitsk, Russia.
[h] INRS — Energie et Materiaux, Varennes, Quebec, Canada.

reduced four-fold, was obtained. A comparison with 2–D fluid simulations shows good agreement when physical sputtering and an ad hoc chemical sputtering source (0.5%) from the private flux region surface is used.

# I. INTRODUCTION

Finding a technique which reduces the high target plate heat flux predicted to occur in future tokamak divertor scenarios continues to be one of the important research areas on tokamaks worldwide. This has been identified as a critical design issue for ITER.[1] A promising solution is to increase the radiation in the divertor legs, thereby reducing the peak heat flux to the target plates and spreading the exhaust power over a large area in the divertor. This regime is desirable because the design requirements for removing the heat flux averaged over a large surface area in the divertor are manageable; robust designs for removal of the predicted peak flux without radiation (up to 10× higher) are very difficult.

Experiments in DIII–D have demonstrated such an increase in radiation and corresponding decrease in target plate peak and integrated heat flux by injection of deuterium gas during the discharge.[2,3] Divertor plasmas, which are detached in these radiative divertor experiments, are characterized by: (1) low $T_e = 1 - 4$ eV and high $n_e > 10^{20}$ m$^{-3}$, (2) enhanced divertor radiated power and $D_\alpha$ emission, (3) a reduction in plasma pressure from the midplane to the divertor along flux surfaces just outside the separatrix, and (4) reduced local heat and particle flux to target plates along those same flux surfaces. Radiation profiles[4] during radiative divertor operation show a strong increase in radiated power in the outboard leg and X–point region compared with profiles in standard ELMing H–mode without deuterium injection.

Radiative divertor conditions were also obtained by injection of gaseous impurities into the divertor. Steady-state radiative divertor plasmas induced by neon and nitrogen injection have achieved peak target heat flux reduction comparable to deuterium-induced radiative divertor plasmas (up to factors of 2.5× with neon and 4× with nitrogen).

Results from recent experiments and modeling of these plasmas in DIII–D are presented below. In Section 2, the experimental procedures to characterize the two-dimensional (2–D) structure of the radiative divertor plasma are presented. Section 3 gives the experimental observations covering the bulk of the lower divertor, including $n_e$ and $T_e$ from the new divertor Thomson system, radiation profiles from bolometry and an evaluation of the constituents which produce the total radiated power from spectroscopy. Section 4 discusses the implications of the measurements for the physical processes dominating detachment, and simulations of these conditions using the UEDGE 2–D SOL and divertor fluid code which support these interpretations. Conclusions are presented in Section 5.

## II. EXECUTION OF EXPERIMENTS

In a recent experimental campaign, we have systematically measured the 2–D (R,Z) structure of the divertor plasma from the inner strikepoint (ISP) to outside the outer strikepoint (OSP) and from the target plates to above the X–point. All discharges in this campaign were lower single-null plasmas with plasma current ($I_p$ = 0.9 to 1.5 MA), toroidal field ($B_t$ = 2.1 T), injected power ($P_{inj}$ = 1 to 10 MW), and safety factor ($q_{95}$ = 3.7 to 6.6). The nominal plasma had the $\nabla B$ drift toward the divertor although approximately 30 discharges were done with reversed toroidal field. Many of the discharges were repeated several times with divertor spectrometers tuned to different spectral regions to obtain data on many radiating charge states for a given plasma condition.

The data set generated from this campaign includes core $n_e$, $T_e$, and $T_i$, from Thomson scattering and CER systems, respectively, and divertor $n_e$, $T_e$ from a new divertor Thomson scattering system[5] (DTS), and from a reciprocating probe in the divertor. Radiated power is determined in 2–D by tomographic reconstruction of data from a 48-channel bolometer system with crossed views. Recycling fluxes are obtained from absolutely calibrated $D_\alpha$ monitors, and target plate heat and particle fluxes are measured by IRTV and Langmuir probes, respectively. Data on

impurity behavior is obtained from images of visible emission lines using tangentially and vertically viewing video cameras, chordal views by multiple visible spectrometers, and absolutely calibrated UV spectrographs with 1 Å resolution in the core and divertor. The configuration of the divertor diagnostics is shown in Fig. 1.

Radial sweeps of the divertor plasma were used to allow diagnostics with vertical views to sample large fractions of the divertor plasma. The nominal equilibrium had the X–point height above the vessel floor, $Z_x$ = 15 cm, elongation, $\kappa$ = 1.7 to 1.9 and triangularity, $\delta$ = 0.3 to 0.55 (large variation during the sweep). During most of the discharges, the divertor strikepoints were swept radially by as much as 25 cm and the X–point moved as much as 18 cm while the shape and position of the core plasma and upper SOL were held constant (R = 1.7 m, a = 0.6 m). Divertor cryopumping was not done in this campaign.

It is assumed that conditions in the divertor remained nearly constant as the plasma is moved since the configuration is essentially an open divertor on horizontal targets without pumping throughout the sweep. Several discharges with a double sweep were checked in detail for hysteresis effects. The macroscopic conditions (e.g., $\bar{n}_e$, total radiated power, ELM frequency) were very reproducible. The constancy of microscopic parameters in the divertor during the sweep is difficult to ascertain, but data from "wide angle" diagnostics, such as filtered video cameras, suggest that the constancy of the divertor was also reasonable except when the OSP location exceeded the radial location of the divertor bias ring face (see Fig. 1). Data from the extreme outward positions of discharges are not included in the analysis here.

Experiments were done with plasmas in Ohmic (O), L–mode (L), ELMing H–mode (H), and reversed $B_t$ operation ($\nabla B$ drift away from the X–point). In addition, plasmas with a radiative divertor induced by $D_2$ injection and with impurity injection (neon and nitrogen) were studied. This paper will focus on comparisons of the 2–D characteristics of ELMing H–mode plasmas with and

without a radiative divertor condition induced by deuterium or impurities. Results from the other operating modes are presented elsewhere.[6–9]

Most of the discharges in these experiments had the X–point positioned at a height $Z_x$ = 15 cm above the divertor floor. This equilibrium produced a poloidal outer leg length of approximately 20 cm from the X–point to the OSP. The maximum radial sweep at constant $Z_x$ with the OSP on the flat divertor floor and not under the bias ring allowed vertically viewing diagnostics to sample the plasma from the X–point to outside the OSP. To increase the coverage of the outer leg by the bolometers, some discharges were run with substantially higher $Z_x$ giving 30 and 50 cm outer leg length (4 and 5 horizontal chords viewing the outer leg, respectively). Radial sweeps with the OSP remaining on the divertor floor were not possible in these discharges.

## III. EXPERIMENTAL OBSERVATIONS

For the first time on DIII–D, these experiments included direct measurements of the plasma characteristics in the bulk of the SOL and divertor during radiative divertor operation. Additional 2–D information was generated by combining several of these measurements. For example, measurements of the divertor electron temperature were combined with spectroscopy measurements and line ratio techniques to determine the spatial location of the radiation.[10,11]

New findings include the first measurements of the electron density, temperature, and pressure in the bulk divertor plasma during radiative divertor operation showing that a large volume of the plasma is cold (~1 to 3 eV) and at high density (1 to 3 $\times$ $10^{20}$ $m^{-3}$).[9] Calibrated spectroscopy measurements showed that carbon is the dominant radiating species near the X–point in PDD plasmas but hydrogenic radiation near the OSP also contributes.[11] In the high X–point experiment, uniformity of radiated power ($P_{rad}$) along the outer leg (within a factor of 2) was verified during radiative divertor operation with peak heat flux on the divertor target reduced a factor of 4.

## A. Divertor Thomson scattering measurements

The divertor Thomson scattering diagnostic measures the $T_e$ and $n_e$ at eight vertical positions above the vessel floor every 50 ms during these discharges (Fig. 1). By sweeping the divertor plasma radially, these measurements sample a large fraction of the divertor plasma and private flux volumes. Using the equilibrium constructed by the EFIT code[12] at each measurement time, each measurement is assigned a poloidal flux value ($\Psi$) and the distance of the point from the target plate along a flux surface, ($L_{pol}$). A 2–D profile is then constructed by remapping each measurement to the (R,Z) location in a representative equilibrium corresponding to the assigned ($L_{pol}$, $\Psi$). Identically prepared discharges with and without deuterium and impurity injection were produced for comparisons.

### 1. Low temperature and high density during PDD

The electron density, temperature, and pressure during the ELMing H–mode before and during the radiative divertor with $D_2$ injection are compared in Fig. 2. In ELMing H–mode, the density rises toward the target plate to 3× the midplane value and the temperature decreases by the same factor. This is consistent with low radiation power and heat flow dominated by parallel heat conduction.[13,14] The electron temperature is greater than 10 eV throughout the divertor and the poloidal gradients are consistent with the conduction limited regime. After the transition to a radiative divertor condition induced by $D_2$ puffing, $T_e$ in a large fraction of the divertor drops to 1 to 3 eV and the poloidal gradients are small. Most of the temperature drop occurs at or above the X–point. Parallel conduction no longer dominates the heat flow throughout the divertor. Density rises to large values (up to $5 \times 10^{20}$ $m^{-3}$ was observed) in the outer SOL, but it rises proportionately less near the separatrix. The peak density on flux surfaces near the separatrix occurs near the X–point (up to 10× the midplane value) falling to near the midplane value at the OSP. The peak density in the outer SOL occurs near the target plate (again at up to 10× the

midplane value). The implications of these conditions, in particular the low temperatures are discussed in Section 4.

## 2. Pressure balance

During both ELMing H–mode and L–mode, the poloidal pressure is constant to within a factor of 2 along all flux surfaces in the SOL.[8] Poloidal profiles of the electron density, temperature, and pressure near the separatrix and farther out in the SOL during radiative divertor operation in an L–mode discharge without ELMs are shown in Fig. 3. The pressure drops by a factor of 5 from the X–point to the target plate on flux surfaces near the separatrix. The radial profile of the pressure shows higher pressure (by a factor of 3 to 5) on flux surfaces in the outer SOL than on those close to the separatrix, confirming observations made previously with probes.[3] The poloidal pressure profile on the outer flux surfaces is roughly constant from the X–point to the target plate.

## B. Radiation profiles

The 2–D profile of the total radiated power, $P_{rad}$, was generated by tomographic reconstruction of data from two 24-channel bolometer systems. Combining the divertor Thomson $T_e$ measurements with line ratio techniques using the divertor VUV SPRED measurements allowed the vertical and horizontal extent of the radiating regions of various hydrogenic and impurity emissions to be calculated. This spatial distribution was verified with images from tangentially and vertically viewing camera systems with visible line filters, and with multi-chord visible spectrometers.

## 1. Power balance

A comparison of the $P_{rad}$ profile during the ELMing H–mode and radiative divertor phases of a deuterium-induced radiative divertor discharge is shown in Fig. 4. The radial profile of the heat flux to the divertor target plates is also shown. During unpumped ELMing H–mode, the radiated power peaks in the inner divertor leg in a region which extends part way up the leg toward the X–point. The heat flux to the inner target is low, consistent with the picture that the power entering the inner leg is radiated away before reaching the plate. The heat flux to the outer target is large, especially in a narrow layer near the separatrix, and little radiated power is seen in the outer leg. Table I gives the power balance for the ELMing H–mode showing that 75% of the input power is accounted for experimentally.

After the transition to PDD operation, the radiated power increases throughout the divertor. The outer leg radiation increases by the largest factor (locally up to factors of 20). The peak is located in the outer leg and also in the vicinity of the X–point. The peak heat flux to the outer target is typically reduced a factor of 3 to 5 as in this discharge and the integrated heat flux to the outer target is reduced a factor of 1.5 to 3. The power accountability (83%) for the radiative divertor phase of this discharge is also given in Table I.

## 2. Constituents contributing to $P_{rad}$

By sweeping the divertor plasma through the field of view of the divertor VUV SPRED spectrograph, the contributions of various radiating species to the total radiated power can be determined throughout the outer divertor leg. To calculate the total radiated power from various species, collisional radiative modeling[15,16] is used to relate radiative intensity of lines within the SPRED range to strong radiating lines outside the range. Good quantitative agreement (within a

factor of 2) is obtained between the total radiated power deduced from SPRED and power measured by a bolometer chord along a similar line of sight.[10]

The fractions of the total radiated power measured by the divertor SPRED are shown for CII, CIII, CIV, and Deuterium in Fig. 5(a) as functions of time during the radiative divertor phase of a discharge with a divertor sweep. The radial position of the OSP is also shown. CIV is the dominant radiator (70% of the total) when the SPRED views the X–point ($R_{OSP}$ ~160 cm) with small contributions (15%) from CIII and deuterium. However, when the instrument views the OSP region ($R_{OSP}$ ~144 to 152 cm) the CIV fraction drops to 40% and the deuterium fraction increases to 45% of the total radiation. Carbon radiation appears to reduce power flow near the X–point; deuterium further reduces power reaching the target plates by radiating near the strikepoint.

Measurements of line ratios from multiple lines of several of these constituents produced estimates of the effective electron temperature at the radiation location. Since the SPRED vertical chord has a similar view to the Thomson scattering $T_e$ measurement, the vertical location of the radiating region can be estimated by interpolating within the eight Thomson points [see Fig. 5(b)]. When radiative divertor operation begins at 3500 ms, the region of significant radiated power from carbon within the field of view of the SPRED shifts up to the X–point (vertical location ~ – 122 cm). In addition, the location of the radiation from the dominant radiator, CIV, is within 1 to 2 cm of the radiation from CIII throughout the discharge. This means that 2–D images of the strong CIII visible line (465 nm), measured with CCD cameras, give approximate distributions of the majority of the radiated power from carbon.

## 3. Profiles of constituents

Data from a tangentially viewing CCD camera (TTV) that views the DIII–D divertor[17] is inverted, using reconstruction techniques similar to those used with the bolometer data, to produce

2–D distributions in a poloidal plane of visible emission from several radiating species. Toroidal symmetry is assumed. Profiles from $D_\alpha$ and CIII radiation during the H–mode and radiative divertor phases of a typical discharge are shown in Fig. 6. During the H–mode phase, the $D_\alpha$ emission is located at the ISP and the CIII emission peaks near the X–point in the inner SOL. Substantial CIII emission is also seen along the inner SOL above and below the X–point and somewhat down the outer divertor leg.

After the transition to the radiative divertor mode, the peak in $P_{rad}$ shifts to the outer leg from the X–point to near the OSP. The $D_\alpha$ radiation measured by the TTV peaks near the OSP. The relative emission intensity near the ISP did not change from the H–mode phase, but the intensity near the OSP increased a factor of 4. The CIII emission peaked at the X–point and outer SOL near the X–point. During the transition to a fully developed radiative divertor mode, and in some discharges with moderate deuterium injection, the CIII emission is observed to extend nearly uniformly as much as half way down the outer divertor leg. The profile becomes highly localized near the X–point with heavy deuterium injection. Data from a vertically viewing CCD system confirms the spatial locations of emission from these constituents

## 4. Poloidal uniformity of $P_{rad}$

To explore in detail the poloidal profile of $P_{rad}$ in the outer leg during radiative divertor operation, discharges were created with a very high X–point. The reconstructed $P_{rad}$ profile from one of these discharges is shown in Fig. 7(a). Uniformity of the radiated power density to within a factor of 2 is observed along flux surfaces from the X–point to the target plate. Inversions of CII, CIII, and $D_\alpha$ visible emission from the TTV for a series of identically produced discharges [Fig. 7(b), 7(c), 7(d)] show that the uniform radiated power is produced by a combination of deuterium radiation near the OSP and carbon radiation further up the leg and near the X–point. Divertor SPRED measurements along the divertor leg are not available from these discharges

because the high X–point precludes radial sweeping. However, if one invokes the hypothesis from Section 3.2.3 that the profile of CIII visible emission nearly represents the profile of total radiated power from carbon, then the TTV images are consistent with the hypothesis that carbon dominates the radiation along the upper divertor leg, and deuterium dominates near the strike point.

### C. X–point MARFE versus divertor MARFE

The CIII emission profile during the PDD phase for the discharge shown in Fig 6 can be stable for long times (100s of milliseconds) with core confinement comparable to the ELMing H–mode phase. This has been demonstrated in discharges with injected power as low as twice the L–H threshold power.[8] However, on some discharges with sufficient deuterium injection, the peak in the CIII profile was observed to move inside the separatrix near the X–point late in the discharge. When this occurred, the core confinement decreased substantially (more than a factor of 2). Petrie[8] has labeled the stable state an "divertor MARFE" and the state with degraded core confinement an "X–point MARFE." This X–point MARFE behavior is consistent with a scenario in which the plasma near the X–point cools to $T_e \lesssim 30$ eV where the carbon radiation rate begins to increase with further decreases in $T_e$. This leads to a thermal collapse of the X–point plasma since it is dominated by carbon radiation. The carbon impurity concentration in the core plasma increased substantially after the formation of the X–point MARFE. This may be consistent with reduced screening of carbon influx to the core from the private flux region through the thermally collapsed X–point.

### D. Radiative divertor plasmas with impurity injection

Experiments were also performed on radiative divertor plasmas induced by neon and nitrogen injection into the divertor. Since neon is a fully recycling impurity, only a short puff (~50 to 80 ms) was required to produce peak target heat flux reduction by up to a factor of 2.5×.

Integrated heat flux reduction up to a factor of 1.7× was achieved. Nitrogen is partially recycling and continuous injection was used to achieve a steady radiative divertor condition. Peak and integrated heat flux reduction factors of up to 4× and 3×, respectively, were achieved. In coronal equilibrium, nitrogen is a much more efficient radiator at the DIII–D divertor/SOL density and temperature than is neon.

## 1. Nitrogen-induced radiative divertor plasmas

Reconstruction of the total radiated power from the bolometer during nitrogen-induced radiative divertor plasmas showed that 60% of the radiated power occurred in the divertor. The peak in the radiation profile occurred on the inner SOL side of the X–point and also at the X–point. TTV images of CII, CIII, NII, and NIII in these discharges confirmed that both the carbon and the nitrogen radiation were localized near the X–point. Analysis of SPRED spectra showed good agreement throughout the discharges (better than a factor of 1.5) with the bolometer channel having a similar line of sight. The relative fractions of the total radiated power measured by SPRED for carbon, nitrogen, and deuterium during the radiative divertor phase are given in Table II. Carbon and nitrogen each contribute substantially to the total with insignificant contribution from deuterium. The relative power fractions for the three ionization states contributing to the nitrogen radiation are given in Table III showing that all are substantial radiators.

## 2. Neon-induced radiative divertor plasmas

The peak and integrated target heat flux reduction factors in the neon discharges were approximately a factor of 2 lower than with nitrogen injection. For these unpumped radiative divertor plasmas, reconstruction of $P_{rad}$ shows that the fraction of the total radiated power which is produced, either inside the separatrix in a mantle surrounding the core plasma or in the SOL above the X–point, is higher with neon than with nitrogen (55% compared with 40%). $P_{rad}$ in the divertor

region was maximum near the X–point with substantial radiation also in both divertor legs. TTV images of $D_\alpha$ emission show that it is localized near the ISP. Images of CIII emission show a peak at the X–point with substantial emission approximately half way down the divertor legs. Analysis of SPRED spectra shows good agreement with the bolometer channel (within a factor of 2). In this case, the majority of the radiation in the divertor was from carbon during the radiative divertor operation, a significant contribution was from deuterium, and a little was from neon. The carbon and neon fractions were comparable when the SPRED viewed the X–point. The relative fractions are given in Table IV.

## IV. DISCUSSION

### A. Data analysis

The DTS measurement of $T_e$ = 1 to 3 eV in a large fraction of the divertor volume during PDD operation leads to a different picture of the physics processes which dominate the divertor plasma compared with the SOL plasma. With low temperature (<5 eV) over long poloidal length, charge exchange and ion neutral collisions can dominate over ionization in enough of the divertor leg to remove a large fraction of the plasma ion momentum to the walls. The reduction in ion flux can lead to a long residence time for ions in the 1 to 2 eV region near the plate. At 1 eV and 5 × $10^{20}$ $m^{-3}$ density (typical of the measurements near the plate), three-body recombination rates can exceed ionization rates by more than an order of magnitude leading to complete neutralization of the ion plasma before it strikes the plates. Molecularly activated recombination may also play an important role in the total recombination rate.[18] Simulations with the UEDGE code indicate that the recombination rate can substantially exceed the ionization rate in regions up to 5 cm poloidally off the plates. This explains the observed reduction to near zero in the plate ion saturation current after the transition to detachment.

The other implication of low and fairly uniform divertor electron temperature is reduced conductive heat flow toward the target plate.[13] The power entering the SOL from the core plasma is removed upstream by radiation and by collisions with cold neutrals consistent with the flat poloidal temperature profile. However, the measurements still show non-negligible heat flux to the target plates and, in some cases, radiated power in regions with shallow temperature gradients. The explanation lies in the potential energy convected by the remaining ion plasma flow, despite strong neutral collision rates upstream. Each remaining deuterium ion can release the 13.6 eV ionization energy in the region where it recombines. Radiated power in regions below $T_e = 2$ eV is possible from this collisional-radiative recombination process.

Radiative divertor operation with uniform $P_{rad}$ in the outer divertor leg was demonstrated in these experiments. However, in many cases, highly non-uniform radiation was also observed. Frequently, the peak occurs in the vicinity of the X–point. One of the factors which affects the spatial distribution of $P_{rad}$ is the deuterium injection rate. Sufficient injection rate is required to produce the transition to the radiative divertor mode but a much lower flow is required to sustain the operation in steady state with nearly uniform $P_{rad}$ in the outer leg. It appears that excess gas injection during the radiative divertor phase reduces $P_{rad}$ in the leg and concentrates the radiation at the X–point, resulting ultimately in an X–point MARFE with reduced core confinement.[8]

Injection of gaseous impurities can produce heat flux reduction similar to deuterium-induced radiative divertor plasmas but the physics behind the result can be very different. For nitrogen-induced ERI plasmas, the nitrogen radiates strongly in the vicinity of the X–point leading to the detachment. Strong deuterium radiation is not observed near the OSP as in the case with deuterium injection. This is consistent with lower density at the OSP during detachment in the nitrogen case. When neon is injected, the bolometer inversions show an increase in the power radiated in a mantle surrounding the core plasma just inside the separatrix. This reduces somewhat the power flowing into the SOL from the core. The heat flux reduction factor in these experiments for quasi-steady

plasmas with neon injection is less than with deuterium injection. Attempts to increase the reduction factor by increasing the amount of injected neon produced, for these unpumped discharges, an unstable core configuration with by long ELM-free periods (~100 ms) followed by large ELMs with significant loss of density and stored energy.

## B. Modeling with UEDGE

Simulations with the UEDGE code[23] have reproduced essentially all of the characteristics of deuterium-induced radiative divertor plasmas observed in these experiments. The code contains a two-fluid model of the plasma with multi-species ions including impurities, classical parallel heat flow, anomalous perpendicular transport, and a Navier-Stokes fluid model of neutrals which permits momentum loss by charge exchange and ion-neutral collisions. Previous simulations[11,19-22] using a fixed-fraction model for the carbon density distribution found qualitative agreement with the measurements. In a recent series of simulations, the complete impurity transport model in UEDGE was used for all six charge states of carbon to examine the sensitivity of detached plasma parameters to a simulated chemical sputtering source of carbon atoms from the floor of the divertor in the private flux region. Results from a simulation of discharge 87506 at 3680 ms using 0.5% effective chemical sputtering yield are shown in Figs. 8 and 9.

This multi-species solution reproduces the experimentally observed detachment ($T_e < 5$ eV) of both divertor leg plasmas up to the vicinity of the X–point [Fig. 8(a)]; the fixed fraction model does not [Fig. 8(b)]. The sensitivity study revealed that physical sputtering alone could not produce the total radiated power measured for reasonable sputtering coefficients (≤0.15%). In addition, the simulation with physical sputtering alone would not detach the outer leg more than a few centimeters off the target plate which is not consistent with the measurements.

The chemical sputtering source and the impurity transport model were critical to simulating both the full detachment of the divertor and to simultaneously matching the midplane plasma profiles [Fig. 8(c)]. The match to the heat flux and line integrated $D_\alpha$ measurements in the divertor are within a factor 2 for the inner plate and within a factor of 3 at the outer plate. Some of the discrepancies in the outer heat flux may be due to the fact that the calculated heat flux does not include reabsorbed energy from upstream radiation. At present, there is no deuterium gas puffing source in the simulation. This may produce low $D_\alpha$ emission compared with the data and slightly higher divertor temperature than measured with the divertor Thomson system [Fig. 8(d)].

Poloidal profiles of plasma quantities from the X–point to each target plate, for a flux surface just inside the SOL near the separatrix, are shown in Figs. 9(a) through 9(d). Figures 9(a) and 9(c) show that the thermal electron and ion pressures are nearly equilibrated and uniform along the divertor legs. The change in the total pressure is due to a combination of thermal pressure drop at the X–point and reduction in the ram pressure ($nmv^2$) from charge-exchange and ion-neutral collisions along the legs. This is consistent with $T_e$ in Figs. 9(b) and 9(d) which drops from 50 to 60 eV just above the X–point to 4 eV just below the X–point to near 1 eV at the plate. Ion-neutral collisions should dominate ionization at these temperatures in the divertor legs for moderate neutral densities. Within 5 cm of both plates, Figs. 9(b) and 9(d) also show that the recombination rate exceeds the ionization rate by up to an order of magnitude. This results from the $T_e = 1$ eV, $n_e = 6 \times 10^{20}$ m$^{-3}$ solution near the plates. The density peaking poloidally near the plates is not due to ionization and recycling as it is in attached plasmas. Rather, it results from reduction in the flow velocity due to ion-neutral collisions upstream.

## V. CONCLUSIONS

Characteristics of the bulk divertor and SOL plasmas were measured and analyzed for ELMing H–mode plasmas before and during radiative divertor operation induced by deuterium or gaseous

impurity injection (neon and nitrogen). During radiative divertor operation with deuterium injection, outer leg detachment is achieved with $T_e$ = 1 to 3 eV throughout a large fraction of the outer leg volume. Peak heat flux is reduced a factor of 3 to 5 and the ion saturation current to the target plates is reduced to near zero. Electron pressure along flux surfaces near the separatrix drops a factor of 10 from the midplane to the target plate with a factor of 3 to 5 drop between the X–point and target. The radial pressure profile increases from the separatrix into the outer SOL of the divertor leg. The radiated power in the outer leg can be made uniform (within a factor of 2) by a combination of carbon radiation the X–point and deuterium radiation near and above the OSP. Analysis and modeling of this condition show that it is consistent with a four-component paradigm of outer leg detachment: (1) ionization in the SOL above the X–point leads to plasma flow toward the divertor, (2) carbon radiation near the X–point reduces $T_e$ in the SOL plasma to approximately 5 eV leading to an ionization front below which ionization is minimal, (3) charge exchange and ion-neutral collisions in the SOL below the X–point remove the parallel momentum from the plasma to the walls and further reduce $T_e$, (4) recombination dominates the plasma near the target plates where $T_e \sim 1$ eV leading to low ion current and heat flux to the plates.

In radiative divertor plasmas with nitrogen injection, the intrinsic carbon and injected nitrogen radiate comparable power in the divertor to produce the observed heat flux reduction and detached conditions. In contrast, for radiative divertor plasmas with neon injection, the neon radiates a substantial fraction of the input power in a mantle surrounding the core and in the SOL above the X–point. This leads to reduced power entering the divertor which allows carbon to radiation to increase near the X–point. The combination of neon radiation outside the divertor and carbon near the X–point produces the heat flux reduction observed on the plates.

## ACKNOWLEDGMENTS

This is a report of work supported by the U.S. Department of Energy under Contract No. DE-AC03-89ER51114 and at Lawrence Livermore National Laboratory under Contract No. W-7405-Eng-48.

## REFERENCES

[1]D. Post, K. Borrass, J. D. Callen, S. A. Cohen, J. G. Cordey, F. Engelmann, N. Fujisawa, M. Harrison, J. Hogan, H. Hopman, Y. Igitkhanov, T. Kaiser, O. Kardaun, S. M. Kaye, S. Krasheninnikov, A. Kukushkin, V. Mukhovatov, W. M. Nevins, A. Nocentini, G. W. Pacher, H. D. Pacher, V. Parail, L. D. Pearlstein, L. Perkins, S. Putvinskij, K. Riedel, D. Sigmar, S. Sugihara, D. Swain, T. Takizuka, K. Tani, T. Tsunematsu, N. A. Uckan, J. G. Wegrowe, J. Wesley, S. Yamamoto, R. Yoshino, K. Young, P. N. Yushmanov, and T. I. Participants, "Physics Aspects of The ITER Design," Proc. 14th IEEE/NPSS Symposium on Fusion Engineering, 1992.

[2]T. W. Petrie, et al., Proc. 18th European Conference on Controlled Fusion and Plasma Physics, 1991 Berlin, Germany.

[3]T. W. Petrie, D. Buchenauer, D. N. Hill, C. Klepper, S. L. Allen, R. B. Campbell, A. Futch, R. J. Groebner, A. Leonard, S. Lippmann, M. A. Mahdavi, M. Rensink, and W. P. West, J. Nucl. Mater. Vol. 196–198 (1992) 848.

[4]A. W. Leonard, S. L. Allen, M. E. Fenstermacher, D. N. Hill, C. J. Lasnier, W. H. Meyer, T. W. Petrie, J. G. Watkins, and R. D. Wood, "Radiation Distributions in Detached Divertor Operation on DIII–D," Proc. 22nd European Conference on Controlled Fusion and Plasma Physics, (1995), Bournemouth, United Kingdom.

[5]D. G. Nilson, T. N. Carlstrom, D. N. Hill, C. L. Hsieh, G. D. Porter, R. E. Stockdale, and J. C. Evans, "Divertor Thomson Scattering on DIII–D," Proc. Seventh International Toki

Conference on Plasma Physics and Controlled Nuclear Fusion (ITC-7), (1995), Toki City, Japan, Vol. 19C, Part III (1995) 105.

[6]W. P. West, T. Evans, N. Brooks, M. Fenstermacher, S. Hirshman, R. Isler, T. Leonard, G. Porter, M. Wade, D. Whyte, R. Wood, "Modeling of Impurity Spectroscopy in the Divertor and SOL of DIII–D Using the 1D Multifluid Model NEWT1D," to be published in Proc. 23rd European Conference on Controlled Fusion and Plasma Physics, July, 1996, Kiev, Ukraine.

[7]J. G. Watkins, "Reciprocating and Fixed Probe Measurements of $n_e$ and $T_e$ in the DIII–D Divertor," Proc. 12th Int. Conf. on Plasma Surface Interactions, May 1996, St. Raphael, France; to be published in J. Nucl. Mater. (1996).

[8]T. W. Petrie, S. L. Allen, T. N. Carlstrom, D. N. Hill, R. Maingi, D. Nilson, M. Brown, D. A. Buchenauer, T. E. Evans, M. E. Fenstermacher, R. A. Jong, C. J. Lasnier, A. W. Leonard, M. A. Mahdavi, G. D. Porter, M. R. Wade, W. P. West, "Investigation of Electron Parallel Pressure Balance in the Scrapeoff Layer of Deuterium-base Radiative Divertor Discharges in DIII–D," Proc. 12th Int. Conf. on Plasma Surface Interactions, May 1996, St. Raphael, France; to be published in J. Nucl. Mater. (1996).

[9]S. L. Allen, T. W. Petrie, D. N. Hill, T. Carlstrom, D. Nilson, A. Leonard, D. Ryutov, G. Porter, R. Maingi, M. Wade, R. Cohen, W. Nevins, M. E. Fenstermacher, R. D. Wood, C. Lasnier, W. P. West, and M. Brown, "First Measurements of Electron Temperature and Density with Divertor Thomson Scattering in Radiative Divertor Discharges on DIII–D," Proc. 12th Int. Conf. on Plasma Surface Interactions, May 1996, St. Raphael, France; to be published in J. Nucl. Mater. (1996).

[10]R. D. Wood, R. C. Isler, S. L. Allen, M. E. Fenstermacher, C. J. Lasnier, A. W. Leonard, W. P. West, "Measurements of Divertor Impurity Concentrations on DIII–D," to be published in Proc. 23rd European Conference on Controlled Fusion and Plasma Physics, 1996 Kiev, Ukraine.

[11]M. E. Fenstermacher, R. D. Wood, S. L. Allen, N. H. Brooks, D. A. Buchenauer, T. N. Carlstrom, J. W. Cuthbertson, E. J. Doyle, T. E. Evans, P.-M. Garbet, R. W. Harvey, D. N. Hill, A. W. Hyatt, R. C. Isler, G. Jackson, R. A. James, R. Jong, C. C. Klepper, C. J. Lasnier, A. W. Leonard, M. A. Mahdavi, R. Maingi, W. H. Meyer, R. A. Moyer, D. G. Nilson, T. W. Petrie, G. D. Porter, T. L. Rhodes, M. J. Schaffer, R. D. Stambaugh, D. M. Thomas, S. Tugarinov, M. R. Wade, J. G. Watkins, W. P. West, D. G. Whyte, "Comprehensive 2–D Measurements of Radiative Divertor Plasmas in DIII–D," Proc. 12th Int. Conf. on Plasma Surface Interactions, May 1996, St. Raphael, France; to be published in J. Nucl. Mater. (1996).

[12]L. L. Lao, J. R. Ferron, R. J. Groebner, W. Howl, H. St. John, E. J. Strait, T. S. Taylor, Nucl. Fusion 30, 1035 (1990).

[13]M. A. Mahdavi, S. L. Allen, N. H. Brooks, R. Bastasz, J. N. Brooks, D. Buchenauer, J. W. Cuthbertson, T. E. Evans, M. E. Fenstermacher, D. N. Hill, D. L. Hillis, J. Hogan, R. C. Isler, G. L. Jackson, T. Jernigan, R. Jong, C. C. Klepper, C. J. Lasnier, A. W. Leonard, R. Maingi, P. K. Mioduszewski, R. A. Moyer, L. W. Owen, T. W. Petrie, G. D. Porter, M. E. Rensink, M. J. Schaffer, G. M. Staebler, R. D. Stambaugh, D. M. Thomas, M. R. Wade, W. R. Wampler, J. G. Watkins, W. P. West, D. G. Whyte, C. P. C. Wong, R. D. Wood, and the DIII–D Physics and Operations Teams, "Divertor Plasma Physics Experiments on the DIII–D Tokamak," to be published in Proc. Plasma Physics and Controlled Fusion Research, (1996), (IAEA 1996, F1-CN-64/A4-3).

[14]A. W. Leonard, "Distributed Divertor Radiation Through Convection in DIII–D," to be published in Phys. Rev. Lett. (1996).

[15]L. C. Johnson and E. Hinov, J. Quant. Spectrosc. Radiat. Transfer 13, 333 (1973).

[16]R. C. Isler, R. W. Wood, C. C. Klepper, N. Brooks, M. W. Fenstermacher, A. W. Leonard, "Spectroscopic Characterization of the DIII–D Divertor," to be published in Phys. Plasmas (1996).

[17]M. E. Fenstermacher, W. H. Meyer, R. D. Wood, D. G. Nilson, R. Ellis, and N. H. Brooks, "A Tangentially Viewing Visible TV System for the DIII–D Divertor," Proc. 11th Top. Conf. on High Temp. Plasma Diagnostics, May 1996, Monterey, California; to be published in Rev. Sci. Instrum. (1996).

[18]S. I. Krasheninnikov, A. Y. Pigarov, T. K. Soboleva, and D. J. Sigmar, "Plasma-Neutral Gas Interaction in a Tokamak Divertor: Effects of Hydrogen Molecules and Plasma Recombination.," Proc. 12th Int. Conf. on Plasma Surface Interactions, May 1996, St. Raphael, France; to be published in J. Nucl. Mater. (1996).

[19]G. D. Porter, "Simulation of Experimentally Achieved Detached Plasmas Using the UEDGE Code," Phys. Plasmas, **3**, 1967, (1996).

[20]M. E. Fenstermacher and G. D. Porter, J. Nucl. Mater. 220, 330 (1995).

[21]G. D. Porter, "Divertor Characterization Experiments on DIII–D," to be published in Proc. 23rd European Conference on Controlled Fusion and Plasma Physics, July day, 1996, Kiev, Ukraine.

[22]M. E. Fenstermacher, S. L. Allen, D. N. Hill, A. W. Leonard, C. J. Lasnier, T. W. Petrie, R. D. Wood, N. H. Brooks, D. A. Buchenauer, T. N. Carlstrom, J. W. Cuthbertson, E. J. Doyle, T. E. Evans, P.-M. Garbet, R. W. Harvey, A. W. Hyatt, R. C. Isler, G. L. Jackson, R. A. James, R. A. Jong, C. C. Klepper, M. A. Mahdavi, R. Maingi, W. H. Meyer, R. A. Moyer, D. G. Nilson, G. D. Porter, T. E. Rhodes, M. J. Schaffer, G. M. Staebler, R. D. Stambaugh, R. E. Stockdale, D. M. Thomas, S. Tugarinov, M. R. Wade, J. G. Watkins, W. P. West, D. G. Whyte, "A Comprehensive 2–D Data Set from DIII–D for Edge Theory Validation," to be published in Plasma Phys. (1996) (from vol. 5th PET, 1996).

TABLE I. Power balance for comparable PDD and ELMing H–mode phases of discharge 87638.

| | 2037 ms | 4310 ms |
|---|---|---|
| $P_{input}$ | 4.01 | 4.29 |
| PNBI | 3.6 | 3.6 |
| $P_{oh}$ | 0.41 | 0.69 |
| $P_{rad}$ | 1.49 | 2.58 |
| $P_{core}$/SOL | 0.75 | 1.0 |
| $P_{div}$ | 0.74 | 1.59 |
| $P_{targets}$ | 1.5 | 1.0 |
| $P_{in}$ | 1.5 | 1.0 |
| $P_{out}$ | 0.0 | 0.0 |
| $P_{out}/P_{in}$ | 0.75 | 0.83 |

TABLE II. Fractions of $P_{rad}$ from C, N, and D in a nitrogen-induced radiative divertor plasma.

| | X–point | Divertor Leg | OSP |
|---|---|---|---|
| Carbon | 0.32 | 0.37 | 0.43 |
| Nitrogen | 0.66 | 0.60 | 0.51 |
| Deuterium | 0.02 | 0.03 | 0.06 |

TABLE III. Fraction of $P_{rad}$ from nitrogen charge states in the divertor of the nitrogen-induced radiative divertor plasma of Table I.

| | X–point | Divertor Leg | OSP |
|---|---|---|---|
| NIII | 0.14 | 0.14 | 0.13 |
| NIV | 0.18 | 0.17 | 0.14 |
| NV | 0.32 | 0.29 | 0.24 |

TABLE IV. Fractions of $P_{rad}$ from C, Ne, and D from a neon-induced radiative divertor plasma.

| | X–point | Divertor Leg | OSP |
|---|---|---|---|
| Carbon | 0.45 | 0.60 | 0.60 |
| Neon | 0.45 | 0.20 | 0.10 |
| Deuterium | 0.10 | 0.20 | 0.30 |

## Figure Captions

Fig. 1. Schematic diagram of DIII–D divertor diagnostic views used to obtain the data from the DCX experiments. Also shown are the outlines of the DIII–D divertor floor (carbon tiles), the vertical port in the floor, and the ADP bias ring, baffle plate and cryopump.

Fig. 2. Electron density [(a),(d)], temperature [(b),(e)] and pressure [(c),(f)] in the outer divertor leg during ELMing H–mode [discharges 86885 and 86886, Figs. 2(a) through 2(c)] and deuterium-induced radiative divertor operation [discharges 87163 and 87164, Figs. 2(d) through 2(f)]. Note that the scales have been changed to highlight the structure in the different cases.

Fig. 3. Poloidal profiles of electron density, temperature, and pressure for two values of poloidal flux during PDD operation: (a) $\Psi = 1.000 - 1.002$ and (b) $\Psi = 1.010 - 1.020$. Note that near the separatrix substantial pressure drop (factor of 4 to 5) is observed between the X–point and the target plate. Pressure is roughly constant further out in the SOL plasma.

Fig. 4. Reconstructed 2–D profiles of the total radiated power from the bolometer arrays and the corresponding heat flux profiles at the target plates during the ELMing H–mode (a) and deuterium-induced radiative divertor phases (b) of the discharge. Note the substantial increase of the radiated power in the outer divertor leg during the radiative divertor phase.

Fig. 5. SPRED spectrograph results during the deuterium-induced radiative divertor phase of a shot with a full radial sweep of the divertor plasma. In (a) the fractions of the total radiated power measured by the SPRED for CII, CIII, CIV and deuterium radiation as well as the radial position of the OSP are shown as functions of time. In (b) the inferred vertical positions of CII, CIII, and CIV emissions are show versus time in which the CIII and CIV radiation are within 1 to 2 cm of each other throughout the sweep.

Fig. 6. Inversions of TTV images of $D_\alpha$ [(a),(c)] and CIII [(b),(d)] emission during ELMing H–mode [(a),(b)] and deuterium-induced radiative divertor phases [(c),(d)]. The total radiated power profiles during both phases (see Fig. 3) are consistent with a combination of deuterium emission close to the strikepoints and carbon emission further up in the divertor legs an near the X–point.

Fig. 7. Total radiated power (a) from the bolometers and $D_\alpha$ (b), CII (c), and CIII (d) emission from the TTV for a discharge with a long (50 cm) poloidal length from the OSP to the X–point. The total radiated power is uniform within a factor of 2 along the entire divertor leg. The radiation is composed of emission from deuterium near the OSP and carbon emission in the upper leg and near the X–point.

Fig. 8. 2–D profiles of the electron temperature calculated in UEDGE simulations of DIII–D discharge 87506 at 3680 ms during deuterium-induced radiative divertor operation. The simulation in (a) used a fixed fraction of carbon relative to electron density and no chemical sputtering model, the simulation in (b) used the multi-species carbon transport and a chemical sputtering source. Also shown are comparisons of the simulated midplane profiles of $n_e$ and $T_e$ with the data and the simulated $n_e$ and $T_e$ along the Divertor Thomson line of sight (within the outer SOL for this discharge) with the data. Curves in blue are from the fixed fraction model; curves in green are from the multi-species model. The 2–D profiles show detachment ($T_e < 5$ eV) in both legs from the target plates to the X–point only in the multi-species simulation. Good agreement with the measurements is also achieved both at the midplane and vertically in the outer SOL in this case.

Fig. 9. Variation of pressures [(a),(c)], and $n_e$, $T_e$, ionization rate and recombination rate [(b),(d)] in both the inner [(a),(b)] and outer [(c),(d)] divertor legs for the UEDGE simulation of discharge 87506 with the multi-species carbon model. Pressure drops from the X–point (shaded region) to the target plates by factors of 3 to 4 are calculated, due to a combination of reductions in the thermal pressure at the X–point and reduction in the ram pressure ($nmv^2$) in the divertor leg. Recombination rate exceeds the ionization rate by up to an order of magnitude in regions with $T_e = 1 - 1.2$ eV and $n_e = 6 - 7 \times 10^{20}$ $m^{-3}$.

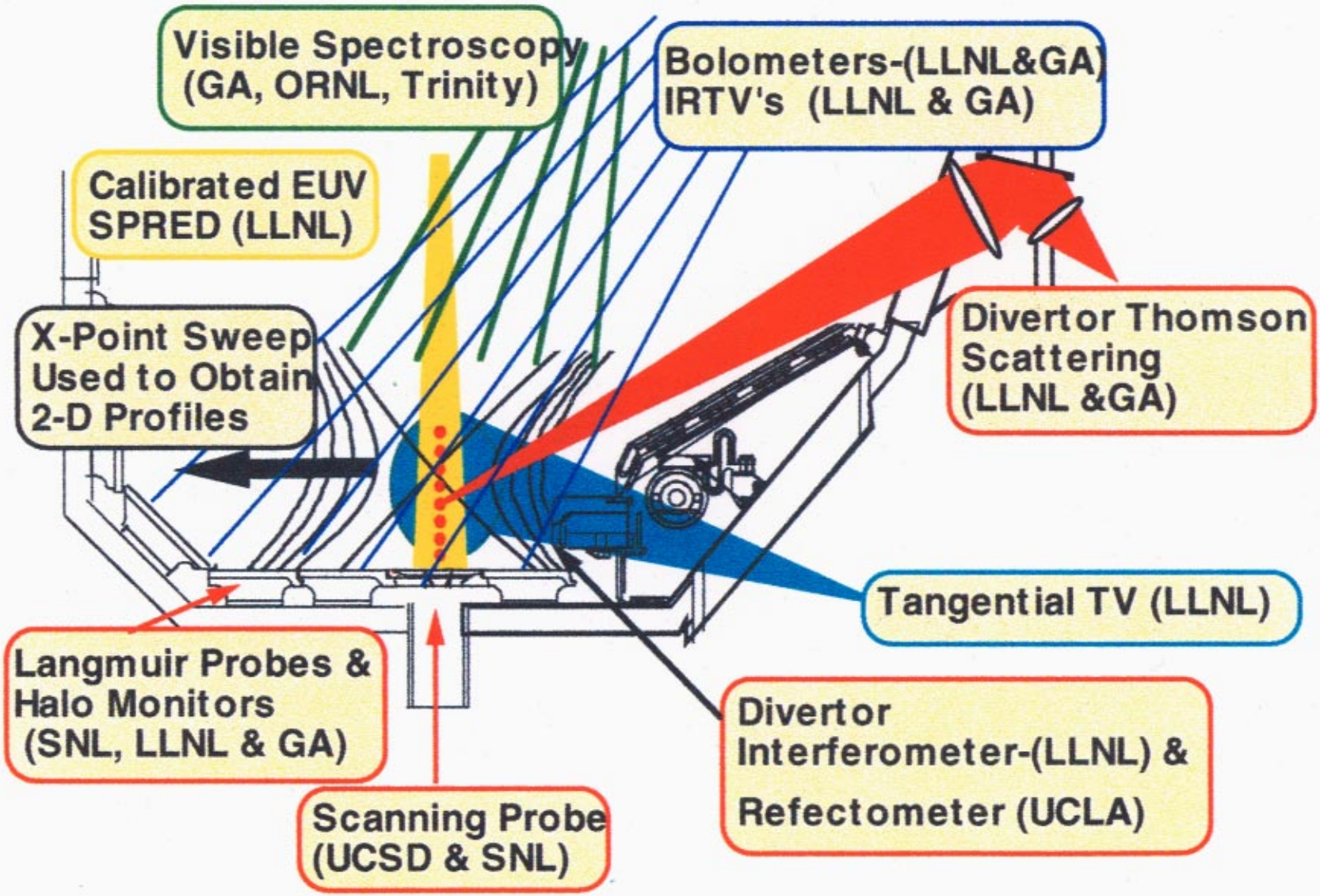


M.E. Fenstermacher, Fig. 1

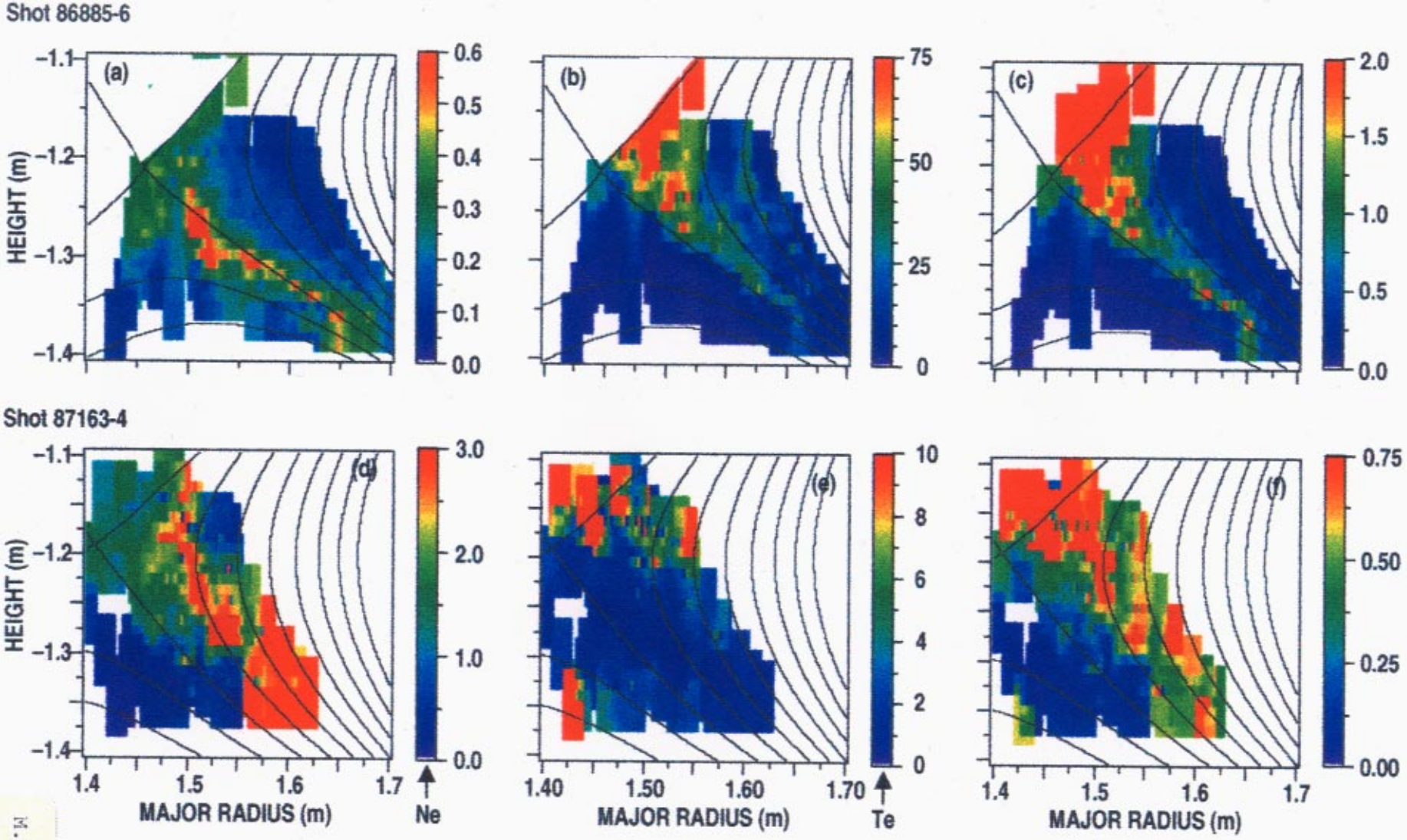


M.E. Fenstermacher, Fig. 2

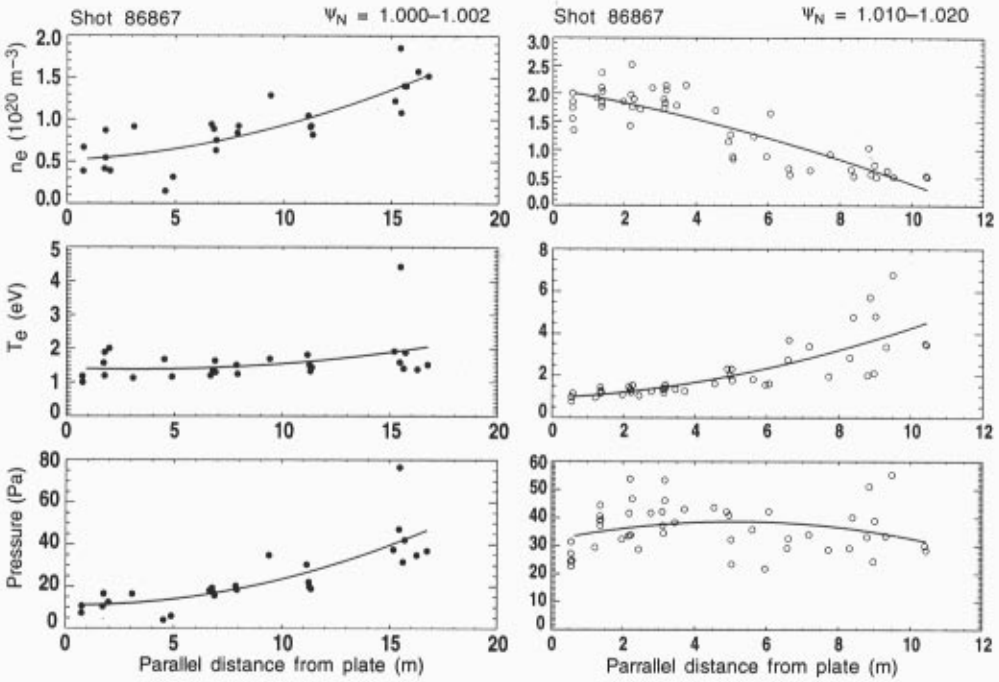


M.E. Fenstermacher, Fig. 3

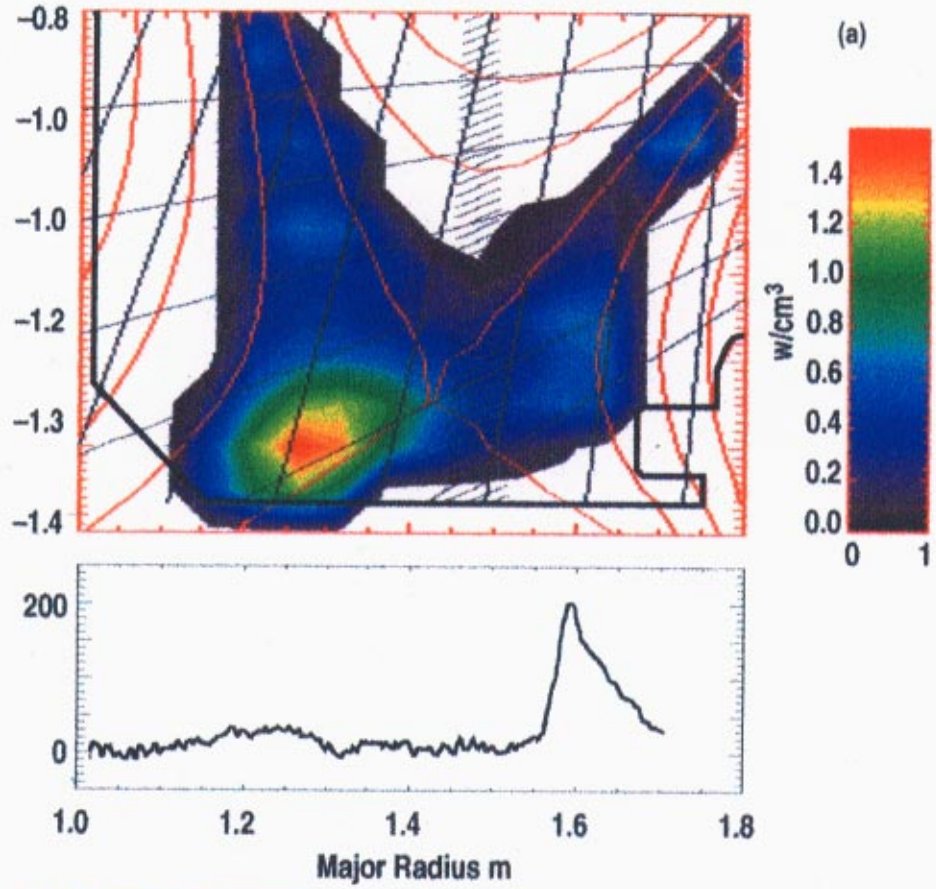


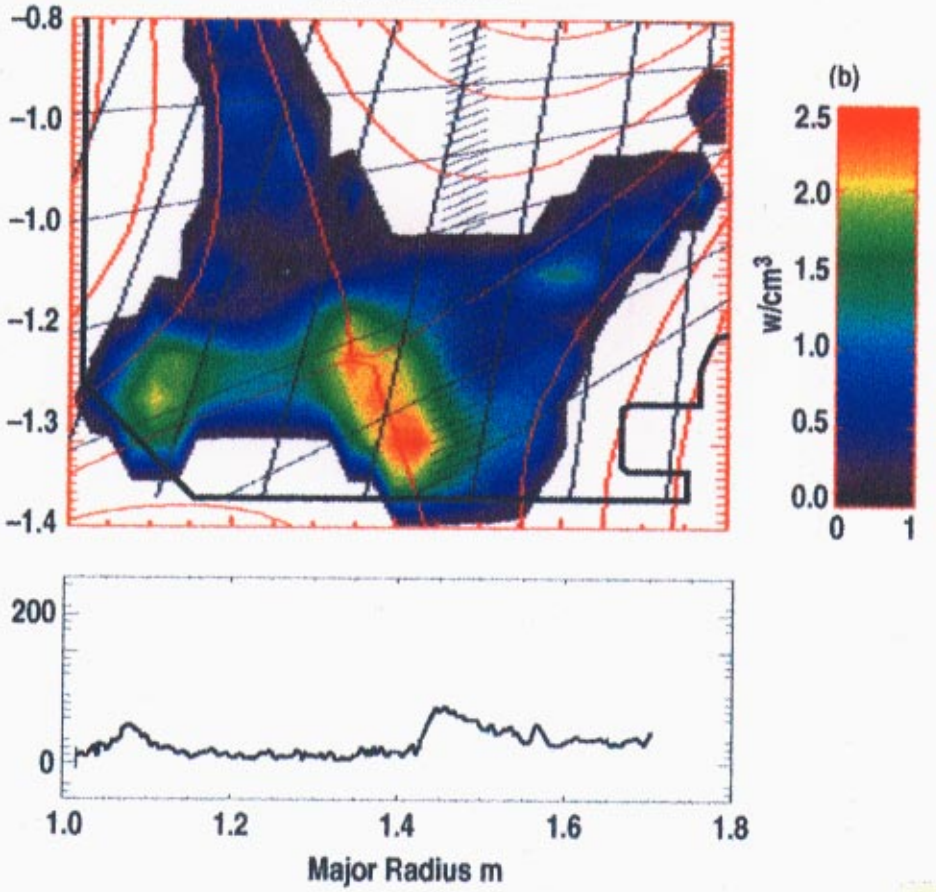


M.E. Fenstermacher, Fig. 4

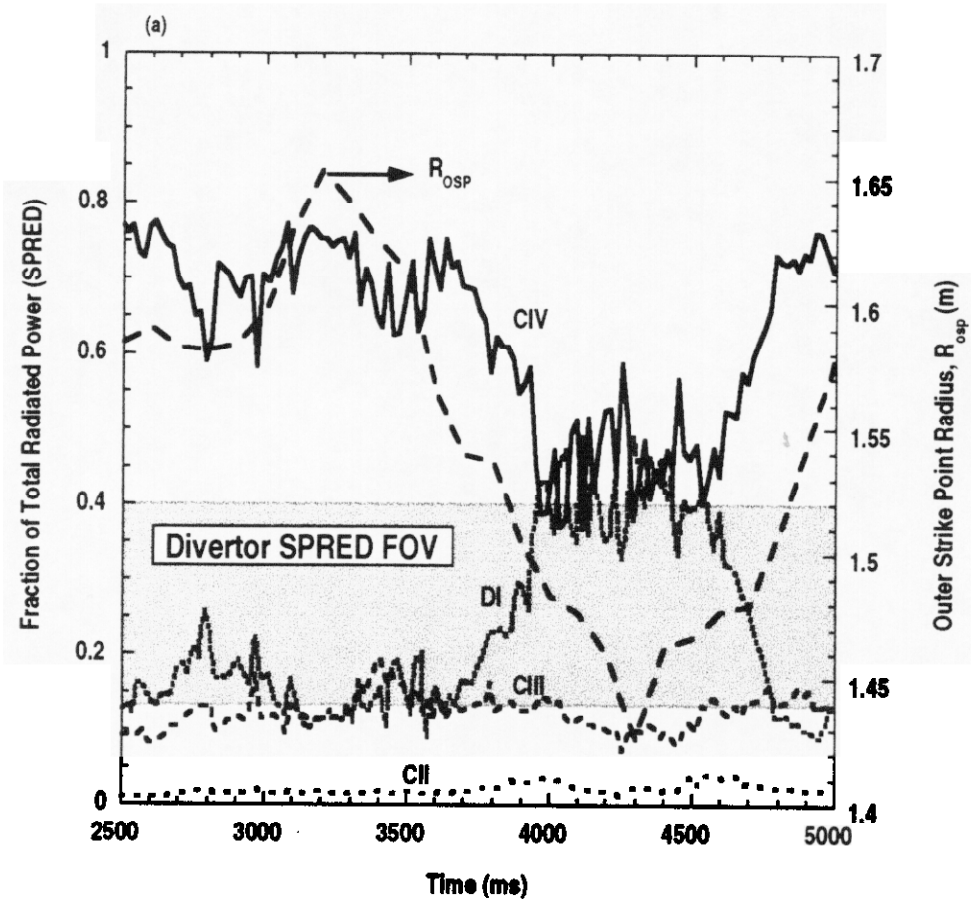


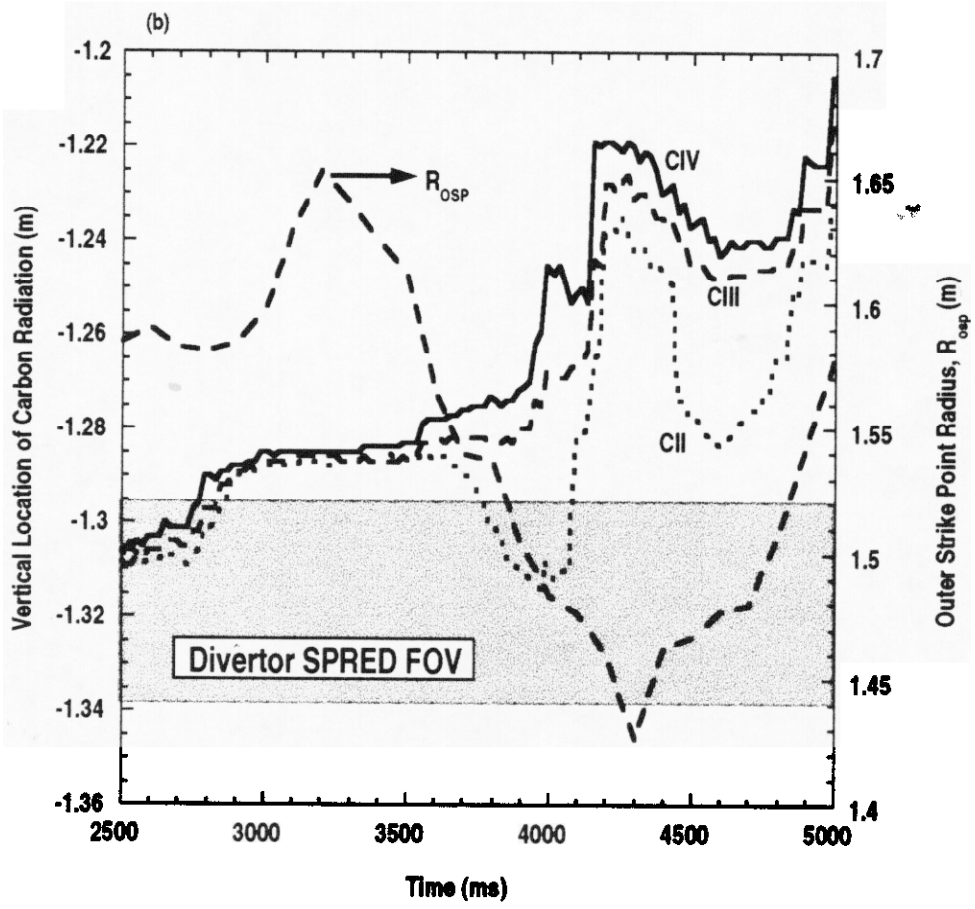


M.E. Fenstermacher, Fig. 5

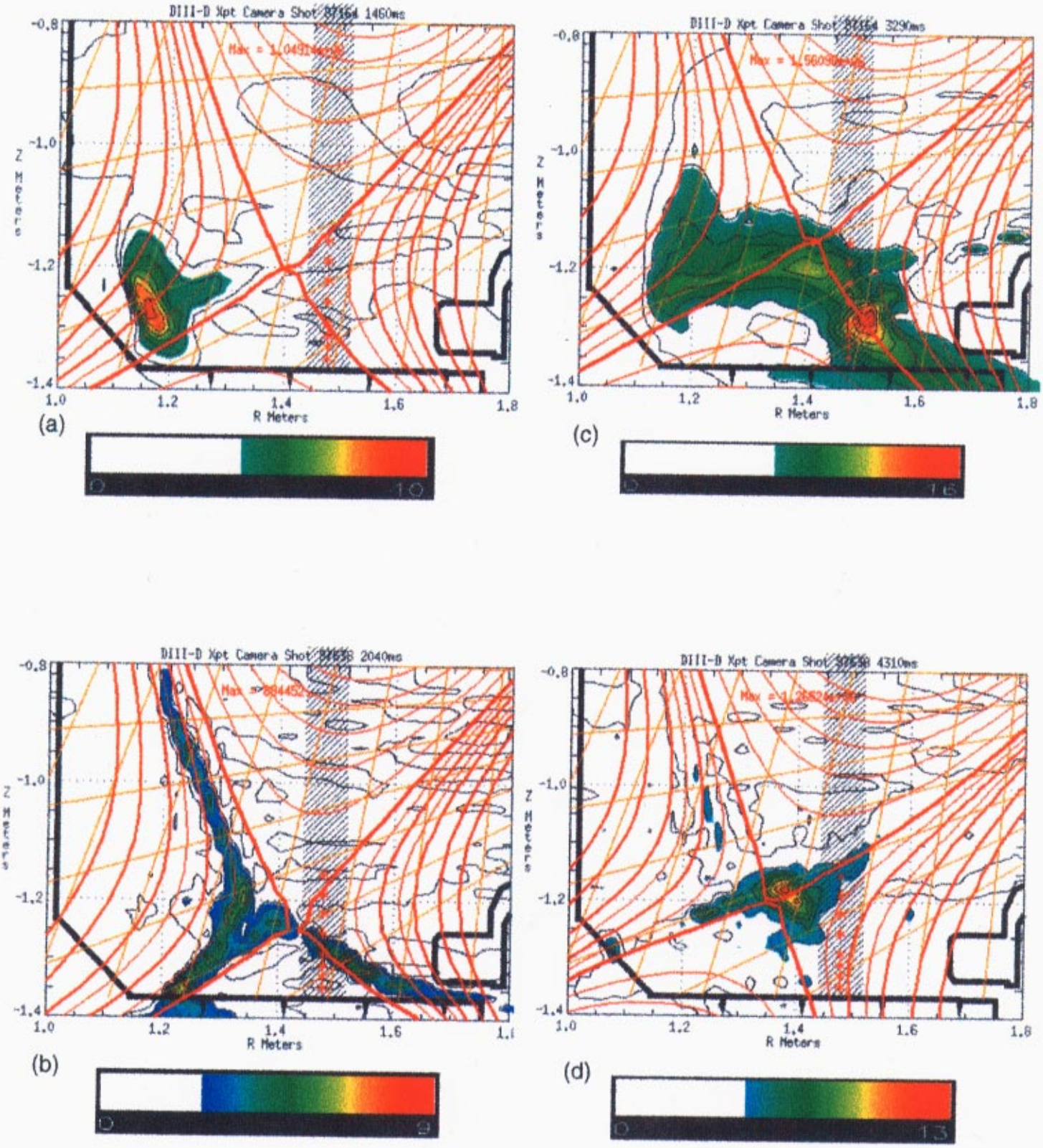


M.E. Fenstermacher, Fig. 6

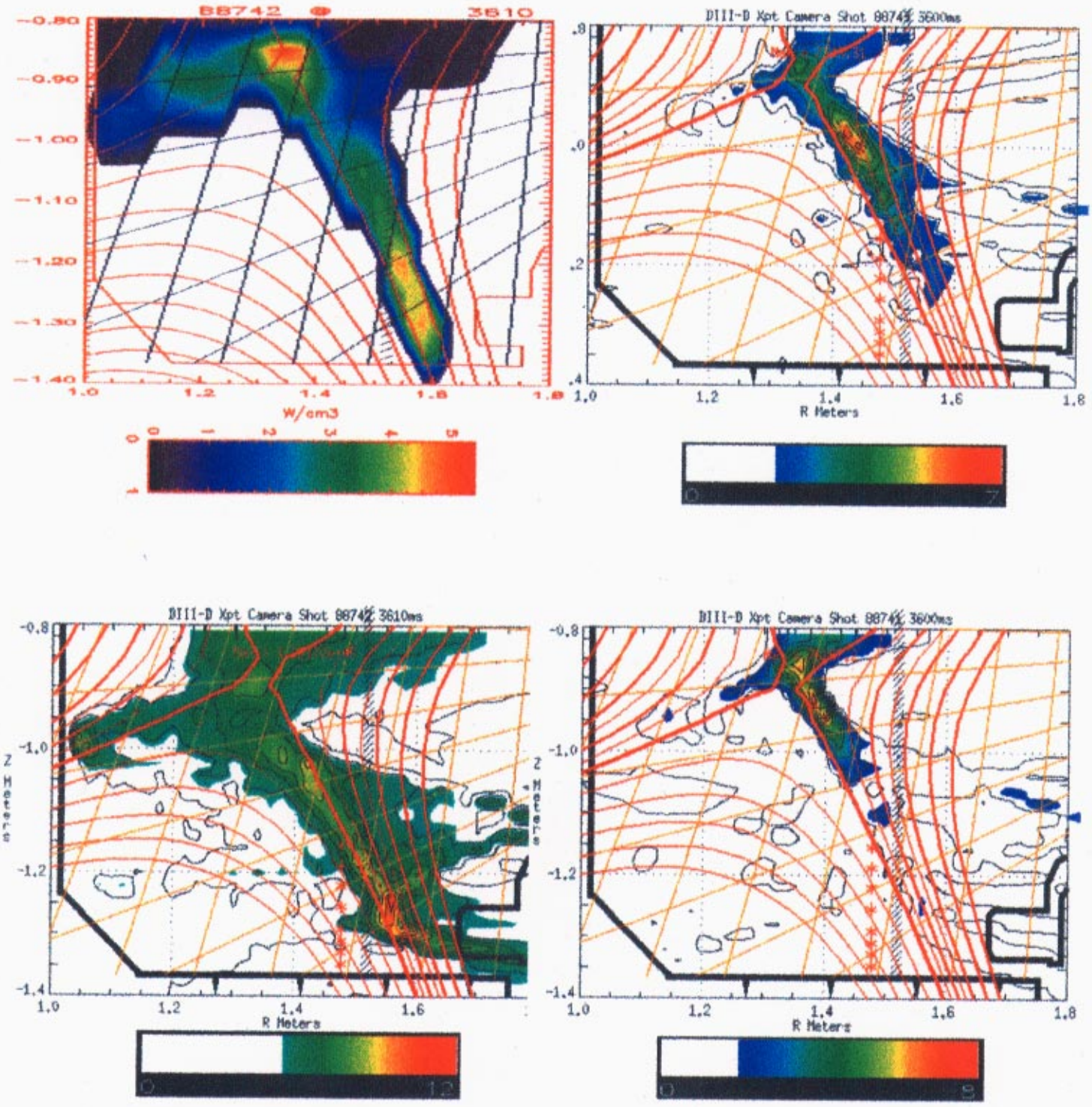


M.E. Fenstermacher, Fig. 7

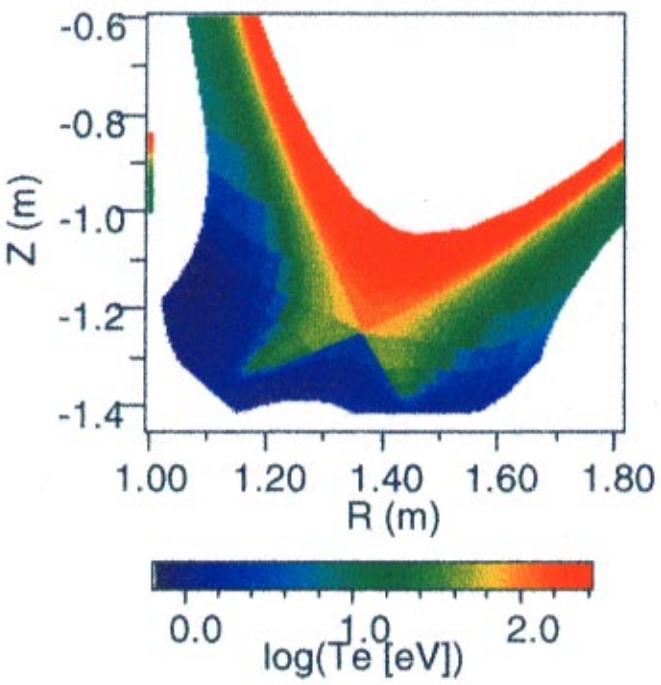
-0.6
-0.8
-1.0
-1.2
-1.4
Z (m)
1.00
1.20
1.40
1.60
1.80
R (m)
0.0
1.0
2.0
log(Te [eV])

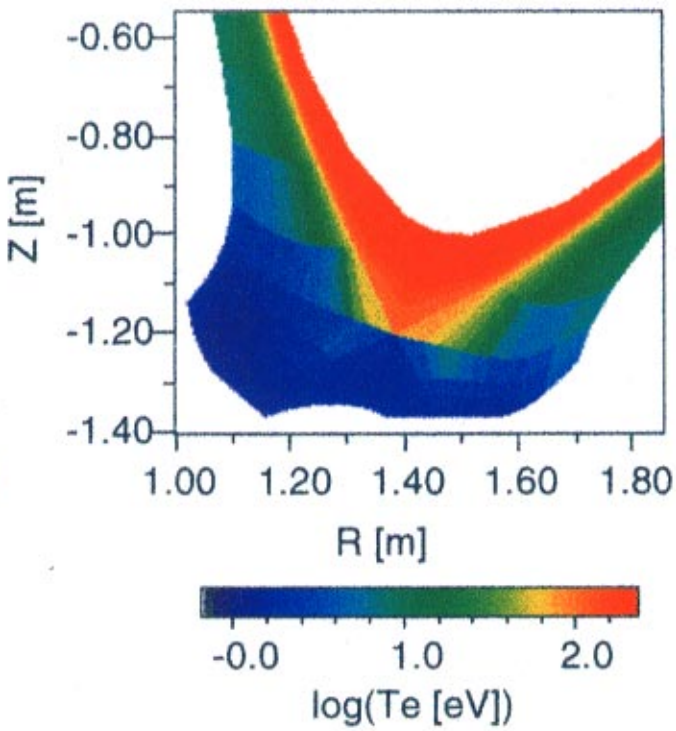
-0.60
-0.80
-1.00
-1.20
-1.40
Z [m]
1.00
1.20
1.40
1.60
1.80
R [m]
-0.0
1.0
2.0
log(Te [eV])

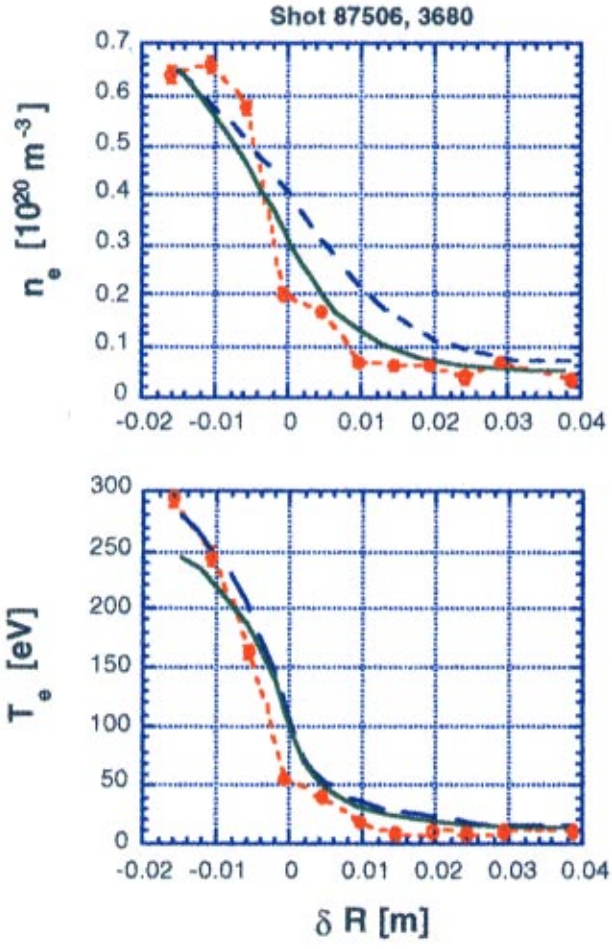
Shot 87506, 3680
$n_e$ [$10^{20}$ $m^{-3}$]
0.7
0.6
0.5
0.4
0.3
0.2
0.1
0
-0.02
-0.01
0
0.01
0.02
0.03
0.04
$T_e$ [eV]
300
250
200
150
100
50
0
δ R [m]

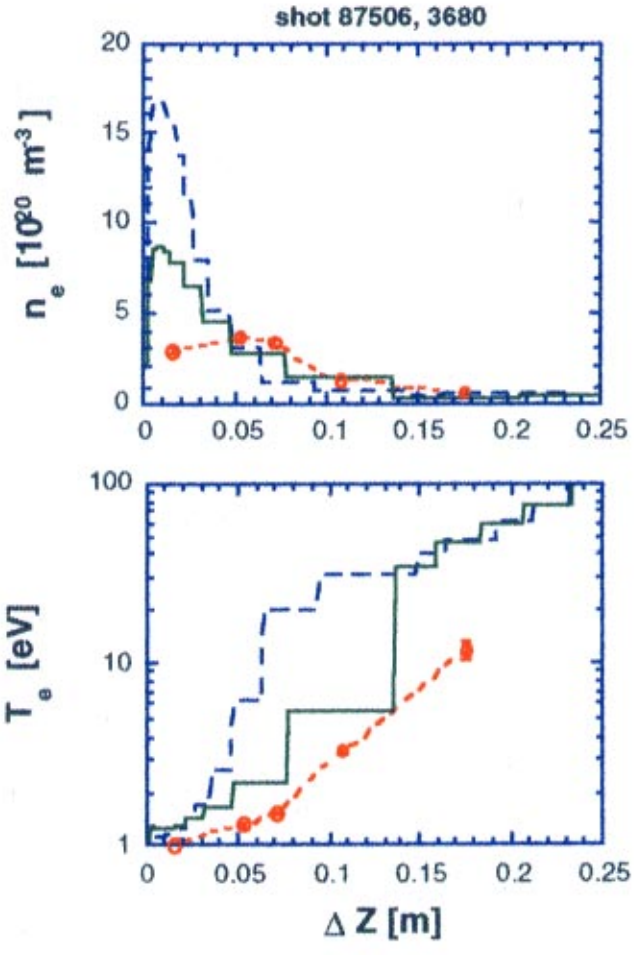
shot 87506, 3680
$n_e$ [$10^{20}$ $m^{-3}$]
20
15
10
5
0
0
0.05
0.1
0.15
0.2
0.25
$T_e$ [eV]
100
10
1
Δ Z [m]

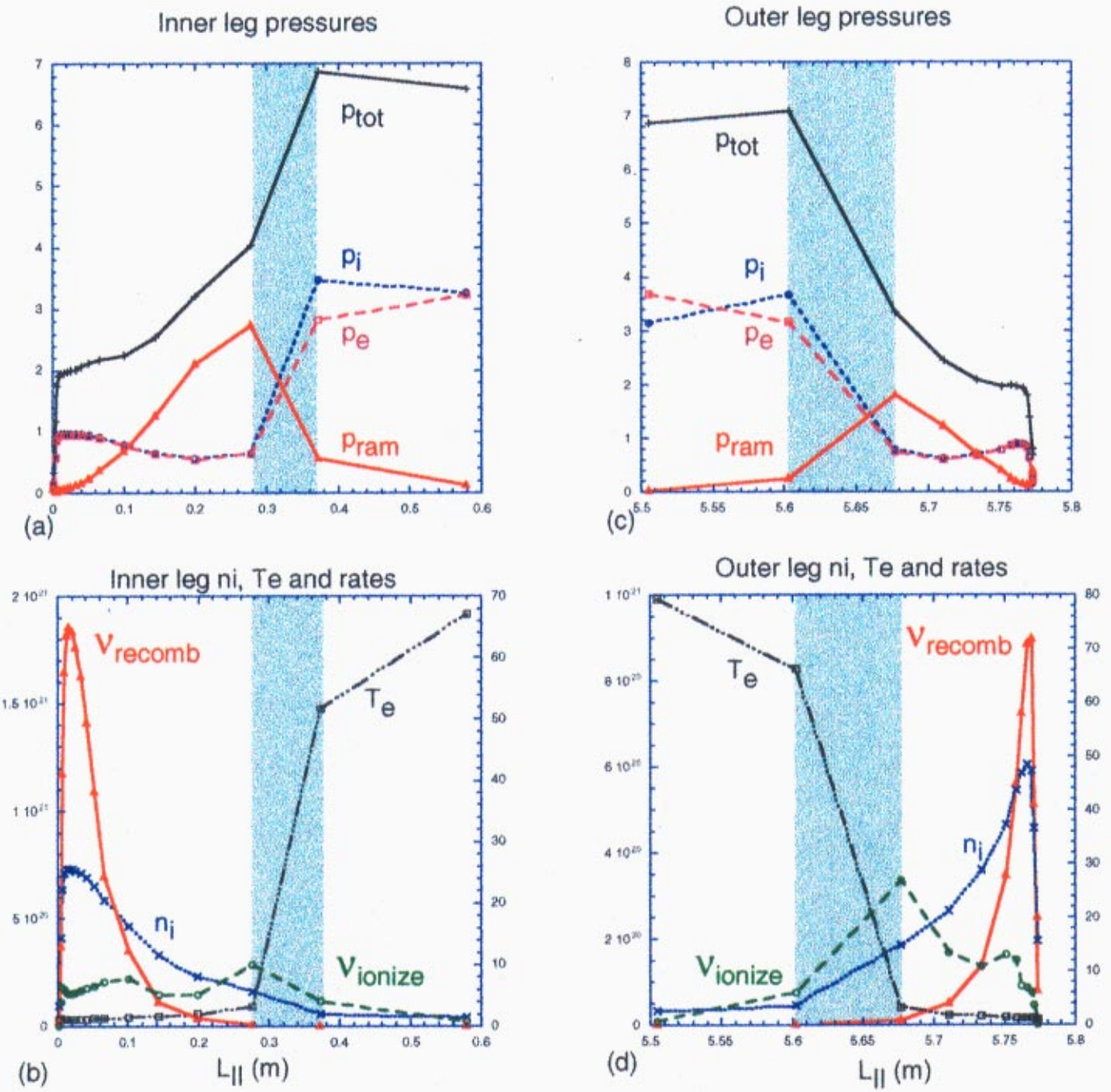


M.E. Fenstermacher, Fig. 9